AAS 26-102

SINGLE-BEACON POSITIONING VIA RADIOMETRY RANGING

Andrea Pizzetti[*], Paolo Panicucci[†], Declan Mages[‡] and Francesco Topputo[§]

Conventional optical navigation techniques extract the line-of-sight from the image of one or multiple target beacons, without using the pixel intensity values other than to find the target centroid. This paper introduces a technique to estimate the range to a known celestial body from the radiometric information contained in the lit pixels of the image. The range, coupled with the estimated line-of-sight, enables a full 3D positioning without a priori state knowledge and using a single image of the target. The method is validated against real flight images taken by the Dawn spacecraft during approach to Vesta and Ceres. Relative range errors below 4% for the former and 1% for the latter are obtained. The magnitude of the relative error is mainly driven by the albedo uniformity and the shape of the target, as confirmed by running the pipeline on synthetic images generated using targets of increasing feature complexity. All in all, these preliminary results demonstrate the feasibility of single-beacon positioning in deep-space and are promising for supporting navigation in celestial triangulation and approach scenarios without the need for redundant sensors.

INTRODUCTION

In recent years, there has been a significant rise in interest in deep-space exploration, leading to an increasing number of missions being launched and many more being proposed. However, the pace of these missions is constrained by the limited availability of ground control resources, which are becoming increasingly saturated. Currently, deep-space missions rely heavily on human operators to manage flight operations throughout every stage of the mission, which adds significantly to the overall costs. As a result, developing autonomous capabilities has become crucial for ensuring sustainable growth and future of deep-space exploration.

Within the navigation task, Optical Navigation (OpNav) stands out as an inexpensive and potentially fully ground-independent solution to determine the spacecraft position by observation of celestial bodies in the Field Of View (FOV) of the camera. The history of missions that used OpNav during cruise and approach to celestial bodies spans from early planetary flybys to modern autonomous rendezvous with moons and small bodies. It began experimentally with the first Mariner missions to Mars, where images of the red planet against the star field were sent to ground to refine the trajectories.[1,2] Galileo, Cassini, and Voyager missions employed ground-based OpNav to improve navigation accuracy during planetary encounters.[3–5] The breakthrough for onboard OpNav came with NASA's Deep Space 1 mission, which demonstrated the AutoNav system to exploit distant asteroid beacons for deep-space cruise, then detect comet Borrelly's nucleus from the image mosaic constructed during the approach.[6] Later, in STARDUST the system was improved to

[*]Ph.D. Student, Department of Aerospace Science and Technology, Politecnico di Milano, Via La Masa 34, 20156, Milan, Italy.

[†]Assistant Professor, Department of Aerospace Science and Technology, Politecnico di Milano, Via La Masa 34, 20156, Milan, Italy.

[‡]Navigation Engineer, Mission Design and Navigation Section, Jet Propulsion Laboratory, 4800 Oak Grove Dr., 91109, Pasadena, CA, United States of America.

[§]Full Professor, Department of Aerospace Science and Technology, Politecnico di Milano, Via La Masa 34, 20156, Milan, Italy.

autonomously track the target in the FOV in the hours preceding the encounter.[7] In the years that followed, many missions such as SMART-1, Rosetta, and Dawn, employed ground-in-the-loop OpNav for navigation to the Moon or small bodies.[8–10] The collision of Deep Impact with comet Tempel 1 was aided by the vision-based navigation system.[11] More recently, DART used autonomous onboard OpNav to lock its terminal trajectory onto Dimorphos.[12] Both Artemis' Orion and JUICE navigation algorithms are based on the extraction and processing of the planet limb for relative state estimation.[13,14] Finally, Hera will employ centroiding and feature tracking for approach and close proximity operations in the Didymos system.[15] The CubeSats that Hera will release to map the binary asteroid environment, Milani and Juventas, will also have their own onboard OpNav system.[16]

Many of these missions triangulated the spacecraft position during interplanetary travel by observing known celestial objects, also called *beacons*, at a far distance. Celestial Triangulation (CT) exploits synchronous measurements of the angles between at least two beacons to estimate the probe state, provided the beacons' positions in an inertial frame are available from e.g. ephemeris. A kinematic (single-epoch) solution of the problem was treated in Ref. 17, then improved and framed in a generalized framework in Ref.[18] Triangulation is typically integrated within a filter to refine the statistical estimation over time, as described in Ref. 19. Using a filter also enables estimation of velocity or other states, with the additional benefit of processing measurements that are asynchronous.[20,21] However, the performance of celestial triangulation is strongly affected by the scene geometry. The more distant the beacon, the higher the induced uncertainty in the estimated position.[22] Triangulation requires good angular separation between the beacons,[22,23] thereby imposing the slewing of the platform for monocular systems, which sometimes can not be accomplished due to operational constraints.[24] Moreover, when planets align one over the other, or when the Sun's location makes pointing to multiple beacons hazardous for the sensor, only one beacon might be actually be observable. Hence, a method capable of retrieving a full position solution from a single image would be highly desirable.

During the approach or flyby trajectory to a planet or small body, a similar need arises. In this phase, the pointing must remain stable to the target, and the Line Of Sight (LoS) measurements are sent to the ground to improve the target ephemeris. This information is typically coupled with Doppler and ranging data from the Deep Space Network (DSN) or ESTRACK to constrain the position of the probe in the along-track direction and to plan trajectory correction maneuvers to target the flyby or rendezvous location.[25] The scenario rapidly changes in terms of target pixel size, and any ground-in-the-loop image processing must be halted 12 to 24 hours before the encounter due to round-trip light-time delays.[26] The pointing guidance commands from that moment on are built using the best available knowledge or refined, switching to a fully autonomous on-board pipeline. In both cases, the availability of a coarse albeit useful range measurement would improve the safety of operations and imaging performance, and possibly avoid using ground-station tracking at all.

Stemming from these needs, this work describes an optical navigation technique that exploits the intensity content of an image to determine the range of a target object from the camera. This information, coupled with the LoS extracted from the image, enables a 3D vector measurement between the observer and the target. To the author's knowledge, it is the first time that the radiometric content of an image is used for a navigation algorithm. Radiometry-informed optical navigation could apply to many scenarios, even not space-related. This article shows how it can be used to approach a celestial body with no a priori information on the probe state, hence without ground-station tracking, and without imposing slewing constraints on the spacecraft, as conventional celestial triangulation would require.

The article is structured as follows. The Methodology section derives the necessary radiometry equations and shows how to retrieve the range and then the position of the observer from the content of an image. In the Experiment section, the feasibility of the technique is assessed using real images taken by the Dawn spacecraft during its approach to Vesta and Ceres, and a synthetic image simulation is carried out to analyze and explain the performance. Concluding remarks are delivered in Conclusions.

METHODOLOGY

The methodology is based on the development of a *measurement model* of the total signal collected by the camera in Digital Number (DN) as an explicit scalar function of the range. The *measurement* is obtained from a simple processing of the image. The range is derived by plugging the measurement into the model and inverting for the range.

The nomenclature used for radiometry quantities in the equations follows the Nicodemus standard[27] and is summarized in Tab. 1. Spectral quantities are labeled by the subscript λ as in Φ_λ.

Table 1: Radiometry nomenclature.

Name	Symbol	Unit of Measure
Radiance	L	$\mathrm{W\,sr^{-1}\,m^{-2}}$
Intensity	I	$\mathrm{W\,sr^{-1}}$
Exitance	M	$\mathrm{W\,m^{-2}}$
Flux Density	F	$\mathrm{W\,m^{-2}}$
Power	Φ	W
Projected Solid Angle	Ω	sr

Measurement Model

The pixel DN values are proportional to the exposure time Δt and the analog-to-digital gain G_{AD}:

$$\mathrm{DN} = \Delta t \; G_{AD} \; \dot{N}_{\mathrm{e^-}} \tag{1}$$

where $\dot{N}_{\mathrm{e^-}}$ is the electron charge rate in $\mathrm{e^-\,s^{-1}}$. This quantity can be written as a function of the spectral power Φ_λ that a pixel collects through the camera pupil:

$$\dot{N}_{\mathrm{e^-}} = \int_{\Delta\lambda} \mathrm{QE}(\lambda)\,\mathrm{T}(\lambda)\,\Phi_\lambda\,\frac{\lambda}{h\,c} \tag{2}$$

where Quantum Efficiency (QE) is the photo-diode conversion efficiency from photons to electrons, Transmittance (T) is the transmission loss of the optical system, and the term $\frac{\lambda}{h\,c}$ arises from the Planck's relation to convert the power from watts to photons per second. The integration limits are given by the bandwidth of the camera filter, i.e. a clear filter will have integration limits across a broad spectrum, whereas a colored filter will have a limited bandwidth. QE and T are usually characterized in pre-flight radiometric calibration at given wavelengths for the different filters to capture the response of the optical system to radiometric stimuli.

The spectral power collected by the pupil is the product of the spectral intensity I_λ reflected by the imaged surface of the celestial body with the projected solid angle Ω subdued to that surface by

the camera:

$$\Phi_\lambda = I_\lambda \, \Omega \tag{3}$$

The reflected intensity is a spectral quantity because the targets generally have different reflection properties depending on the spectrum of observation. The reflection properties at far range can be synthesized by the geometric albedo p_G, defined as the ratio of a body's brightness at zero phase angle to the brightness of a perfectly diffusing disk at the same position and with the same apparent size.[28] Geometric albedos for different bodies of the solar system and at different wavelengths are typically available from on-ground observation campaigns.[29] The spectral intensity reflected by a spherical and point-wise (i.e., $d_{\text{cam}} >> R$) target can be written as a function of the geometric albedo as:[28]

$$I_\lambda = \Psi(\alpha, \lambda) \, R^2 \, F_{\lambda_\odot} \, p_G(\lambda) \tag{4}$$

where $\Psi(\alpha, \lambda)$ is the phase law which defines the attenuation of the brightness at phase angle α and wavelength λ, R is the celestial body radius, $F_{\lambda_\odot}$ is the spectral flux density of the light beams impacting the body. The beams are assumed to arrive parallel, i.e., the light source is very far from the body.

The spectral radiant flux density of a point-wise Lambertian emitter[30] arriving at a point located at a distance $d_\odot$ is:

$$F_{\lambda_\odot} = \frac{4 \, \pi \, R_\odot^2}{4 \, \pi \, d_\odot^2} \, M_{\lambda_\odot} = \frac{R_\odot^2}{d_\odot^2} \, \pi \, L_{\lambda_\odot} \tag{5}$$

where $M_{\lambda_\odot}$ and $L_{\lambda_\odot}$ are respectively the spectral exitance and radiance of the light source, and $R_\odot$ its radius.

Finally, the projected solid angle for a distant point-wise body can be approximated by:[30]

$$\Omega = \frac{A_{\text{cam}} \, \cos \epsilon}{d_{\text{cam}}^2} \tag{6}$$

where A_{cam} is the camera pupil area, d_{cam} is the camera distance from the body and ϵ is the off-pointing angle between the camera boresight and the LoS of the target.

Combining Eqs. (1-6), the following expression is obtained:

$$\text{DN} = \Delta t \, G_{AD} \, \frac{\pi \, R_\odot^2}{d_\odot^2} \, R^2 \, \frac{A_{\text{cam}} \, \cos \epsilon}{d_{\text{cam}}^2} \int_{\Delta\lambda} \Psi(\alpha, \lambda) \, p_G(\lambda) \, \text{QE}(\lambda) \, \text{T}(\lambda) \, \frac{\lambda}{h \, c} \, L_{\lambda_\odot} \tag{7}$$

Eq. (7) is the measurement model of the total DN collected by a camera under the following assumptions:

1. The light source is a single point-wise Lambertian emitter
2. The reflecting body is a sphere with uniform albedo
3. The observer is located at a far distance from the body

These assumptions are often justified in a space environment: the Sun can be modeled as a point-wise Lambertian source due to the large distances involved, many planets and moons are approximately spherical, and spacecrafts typically observe targets from distances that are large compared to the body size. Even when these conditions are not satisfied - for example, during close-approach trajectories to irregularly shaped asteroids - the model can still provide a useful approximation, as it will be demonstrated in the Experiment section.

Range Equation

Provided that the DN measurement can be extracted from the image, the measurement model can be inverted for the range:

$$d_{\text{cam}} = \sqrt{\frac{\Delta t}{\text{DN}} \, G_{AD} \, \frac{\pi \, R_{\odot}^2}{d_{\odot}^2} \, R^2 \, A_{\text{cam}} \, \cos\epsilon \int_{\Delta\lambda} \Psi(\alpha, \lambda) \, p_G(\lambda) \, \text{QE}(\lambda) \, \text{T}(\lambda) \, \frac{\lambda}{h \, c} \, L_{\lambda_{\odot}}} \tag{8}$$

To solve the equation, a partial knowledge of the scene geometry is required: the distance of the body from the Sun $d_{\odot}$, the phase angle α, and the off-pointing angle ϵ. These quantities can be derived without any a priori information on the spacecraft state. In particular, they can be computed from the on-board ephemeris, the measured target LoS, and the estimated spacecraft inertial attitude.

The Sun-body distance $d_{\odot}$ is the norm of the position vector with respect to the Sun in the inertial frame $\boldsymbol{r}_{\odot}^{\text{I}}$, evaluated from the on-board ephemeris at the current epoch:

$$d_{\odot} = ||\boldsymbol{r}_{\odot}^{\text{I}}|| \tag{9}$$

The phase angle α can be obtained as the angle between the Sun-body direction vector in the camera frame $\hat{\boldsymbol{r}}_{\odot}^{\text{C}}$ and the measured LoS vector $\hat{\boldsymbol{l}}^{\text{C}}$:

$$\alpha = \arccos\left(\hat{\boldsymbol{r}}_{\odot}^{\text{C}} \cdot \hat{\boldsymbol{l}}^{\text{C}}\right) \tag{10}$$

where $\hat{\boldsymbol{r}}_{\odot}^{\text{C}}$ is given by:

$$\hat{\boldsymbol{r}}_{\odot}^{\text{C}} = A_{\text{I}\to\text{C}} \, \frac{\boldsymbol{r}_{\odot}^{I}}{d_{\odot}} \tag{11}$$

with $A_{\text{I}\to\text{C}}$ the direction cosine matrix that rotates from the inertial frame to the camera frame, and $\hat{\boldsymbol{l}}^{\text{C}}$ is given by:

$$\hat{\boldsymbol{l}}^{\text{C}} = \frac{1}{\sqrt{\hat{u}^2 + \hat{v}^2 + 1}} \begin{bmatrix} \hat{u} \\ \hat{v} \\ 1 \end{bmatrix} \tag{12}$$

with $\hat{u}$ and $\hat{v}$ the normalized horizontal and vertical coordinates of the Center of Brightness (CoB), namely:

$$\hat{u} = \mu_u \frac{u - c_u}{f} \tag{13}$$

$$\hat{v} = \mu_v \frac{v - c_v}{f} \tag{14}$$

with c_u and c_v the optical center in pixels, μ_u and μ_v the pixel pitch and f the focal length.

Finally, the off-pointing angle ϵ is the angle between the camera boresight ($+Z$ axis of the camera reference frame) and the LoS $\hat{\boldsymbol{l}}^{\text{C}}$. Therefore, the cosine of ϵ is the 3rd component of the LoS vector:

$$\cos(\epsilon) = \frac{1}{\sqrt{\hat{u}^2 + \hat{v}^2 + 1}} \tag{15}$$

The rotation matrix $A_{\mathrm{I}\to\mathrm{C}}$ is assumed to be furnished by the attitude determination and control subsystem, or otherwise estimated from the star pattern using a longer exposure frame with the same camera or with a dedicated star tracker.

Once these geometric parameters have been computed, the solution to Eq. (8) is explicit, provided that the camera has been characterized in terms of QE, T and filter bandwidth and that the body is known in terms of reflection properties and size (i.e., $\Psi(\alpha,\lambda)$, $p_G(\lambda)$ and R).

The estimated range, coupled with the LoS, enables a full 3D relative (camera-to-target) position estimation:

$$\boldsymbol{r}_{+}^{\mathrm{C}} = d_{cam}\,\hat{\boldsymbol{l}}^{\mathrm{C}} \tag{16}$$

as well as absolute (Sun-to-spacecraft), by plugging back the Sun position and the orientation matrix:

$$\boldsymbol{r}^{\mathrm{I}} = \boldsymbol{r}_{\odot}^{\mathrm{I}} - A_{\mathrm{C}\to\mathrm{I}}\,\boldsymbol{r}_{+}^{\mathrm{C}} \tag{17}$$

Therefore, the presented methodology is suitable for single-beacon positioning without any a-priori knowledge of current or previous spacecraft states.

EXPERIMENT

The feasibility of the navigation algorithm is assessed using a dataset of real images taken during the approach to Vesta and Ceres by the Dawn mission.

The Vesta approach dataset covers the 10 OpNav sequences carried out between the 3rd of May and the 24th of June 2011, for a total of 200 images (20 images for each sequence). Each sequence is separated by approximately 1 week and Vesta's apparent diameter in the camera pixel array increases from 4 to 37 pixels between the first and last sequence. The Ceres dataset is smaller and contains 3 sequences for a total of 60 images taken between the 13th of January and the 4th of February 2015. This dwarf planet is much larger than Vesta and its diameter span 26 to 68 px during the approach.

The two celestial bodies have very different characteristics: while Vesta is very bright but irregular, Ceres has a quasi-spherical shape, but its albedo is much lower. Therefore, they are the perfect candidates for testing the methodology across two diverse scenarios and evaluating how far the underlying model assumptions can be stretched.

Parameters Retrieval

To keep the experiment realistic, only pre-arrival parameters were used when available. This includes those estimated during standard in-orbit calibration procedures, before reaching the targets.

The Dawn camera system comprises two identical optical imaging devices (Framing Camera 1 and 2) equipped with one broad-band (clear) filter and seven narrow-band filters. The cameras utilize a TH7888 1024x1024 pixel front illuminated frame transfer CCD detector, sensitive in the 400-1050 nm wavelength. The parameters of Framing Camera 2 (FC2) are reported in Tab. 2.

Instead of using QE and T, which should be independently estimated before-hand, it is convenient to employ the camera responsivity function $\mathrm{S}(\lambda)$, as it embeds them together with other camera-specific parameters. The responsivity function for the clear filter is defined as:[31]

$$\mathrm{S}_1(\lambda) = C_1 \frac{A_{\mathrm{cam}}}{G_{\mathrm{DA}}} \mathrm{QE}\,(\lambda)\mathrm{T}(\lambda)\,\frac{\lambda}{h\,c} \tag{18}$$

where C_1 is the clear filter calibration coefficient found with the first in-flight radiometric calibration in 2012[32] and revised later in 2019.[31] The responsivity before and after calibration is plotted in Fig. 1 as a function of the wavelength. The uncalibrated responsivity ($C_1 = 1$) has been gathered from the pre-launch test campaign documents, for the clear and colored filters.[33]

Table 2: Parameters of Framing Camera 2[31,32]

Name	Symbol	Value	Unit of Measure
Pupil Area	A_{cam}	341	mm^2
Focal Length	f	150	mm
Resolution	res_u, res_v	1024	px
Pixel Pitch	μ_u, μ_v	14	µm
Optical Center	c_u, c_v	$[511.5, 511.5]$	px
Bit Depth	n_{bit}	14	bits
Digital-to-Analog Gain	G_{DA}	17.7	$\mathrm{e^-\,DN^{-1}}$
Bias	$\mathrm{DN}^{(0)}$	269	DN
Responsivity Function	$\mathrm{S}_1(\lambda)$	Fig. 1	$\mathrm{DN\,s^{-1}\,W^{-1}\,m^2}$
Calibration Coefficient	C_1	1.1043	–

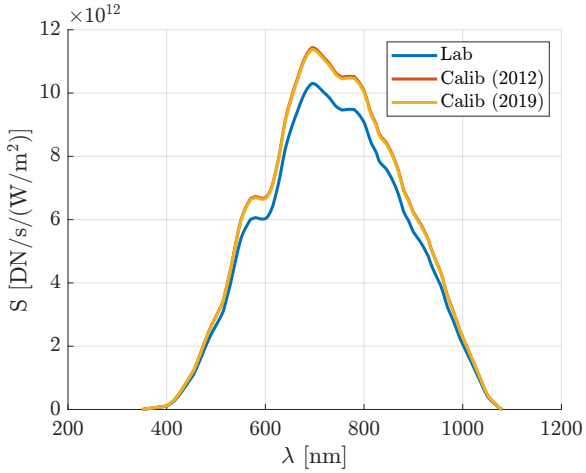

Figure 1: Responsivity of Framing Camera 2. The first in-orbit calibration assessed a change of about 10% with respect to the ground calibration.

Concerning the modeling of Vesta and Ceres, the mean radius, geometric albedo, and Hapke model parameters are reported in Tab. 3.

The geometric albedo in the clear filter is extrapolated from the geometric albedo measurements in the 7 different color filters of FC2[34,35] and depicted in Fig. 2. The extrapolation is carried out by

weighting the integral of the camera responsivity to the Sun spectrum in each filter bandwidth for the corresponding albedo value. The geometric albedo extrapolated in this way already refers to the clear filter bandwidth and is therefore a constant quantity with respect to the wavelength. It can be taken out of the integral in Eq. (8).

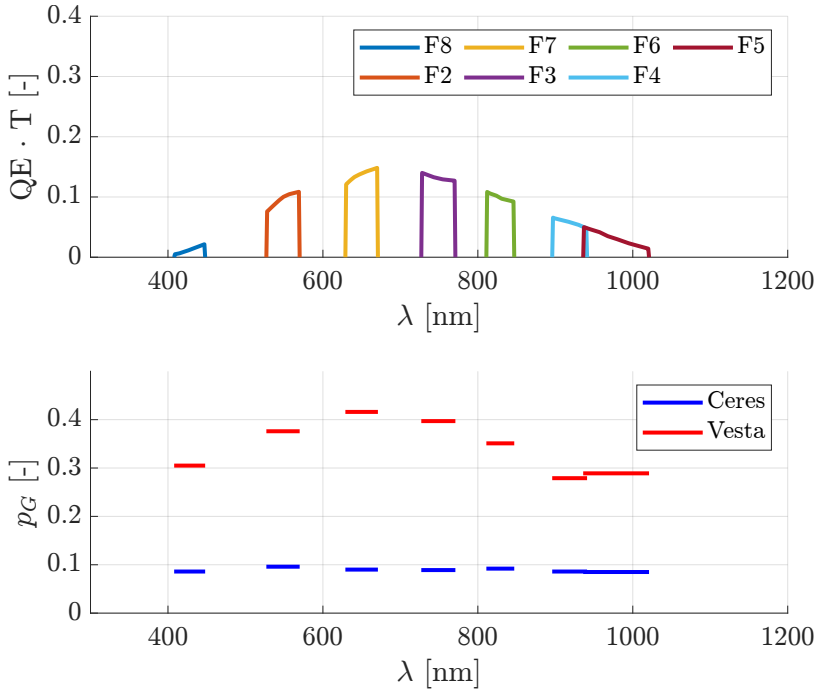

Figure 2: Geometric albedo measurements of Vesta and Ceres in the seven filters of Framing Camera 2

The reflection model considered for both celestial bodies is the Hapke model.[36,37] The phase law for an Hapke model and its component functions are explicitly reported in Appendix A: Hapke Phase Law. The selected Hapke parameters are assumed not to depend on the wavelength throughout the clear filter bandwidth, so the phase law can be extracted from the spectral integral as well.

Table 3: Size and reflection parameters of Vesta[34] and Ceres.[35] Refer to Appendix A: Hapke Phase Law for the explanation of the Hapke parameters.

	$\bar{R}$ [km]	$\bar{p}_G$ [-]	w [-]	b_{HG} [−]	c_{HG} [-]	θ [deg]	B_0 [−]	h [-]
Vesta	255	0.34	0.49	-0.27	-1	18	1	0.054
Ceres	460	0.09	0.14	0.37	0.081	20	1.6	0.06

Image Processing

The DN measurement at each frame is obtained by running a relatively simple Image Processing (IP) pipeline to obtain the center and size of a Region of Interest (ROI).

Firstly, the image is filtered with a box filter of 5 px size to reject cosmic rays and hot pixels. Then, the image is thresholded by discarding the pixels whose value is less than the mean image intensity plus three standard deviations. At this point, all the remaining pixels are grouped into

blobs. The ROI center is found as the center of brightness (based on image moments) of the largest blob, while its size is found as the equivalent radius of a circle with an area equal to the number of pixels in the blob plus a fixed offset of 5 px. Fig. 3 shows the effectiveness of the IP algorithm for a sample frame of 5 different sequences during the Vesta approach.

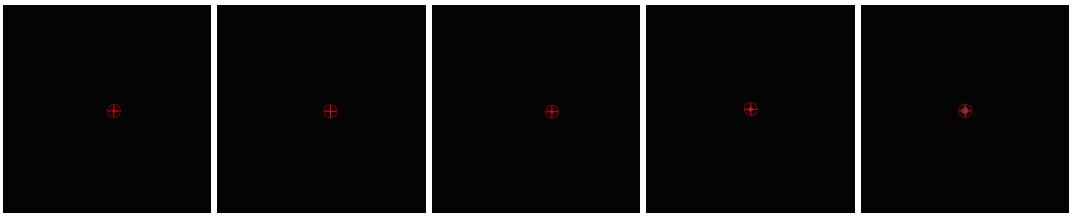

(a) Centroiding

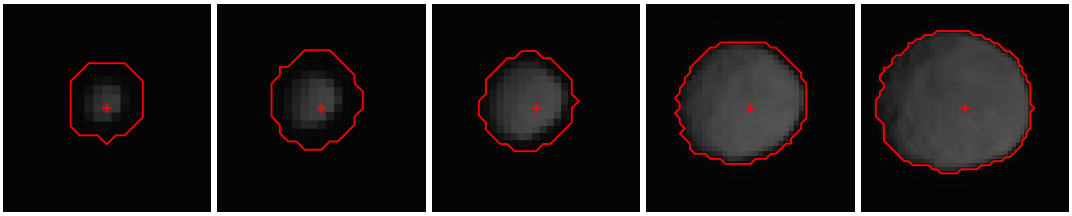

(b) ROI Segmentation

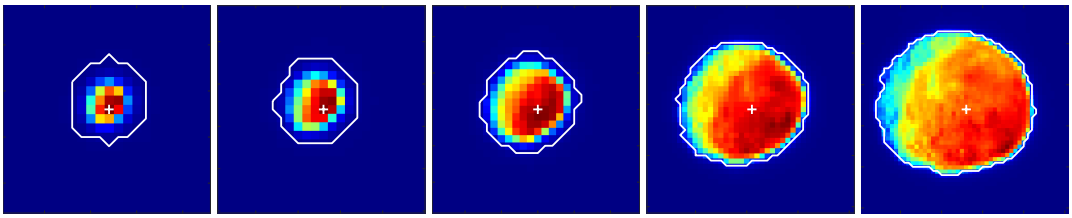

(c) ROI Segmentation (false color)

Figure 3: Image processing of frames belonging to different OpNav sequences taken during the Vesta approach

The intensity of each pixel is affected by several noise and error sources, such as shot noise, dark current, and bias, amongst others. To show the effectiveness of the technique with minimal knowledge of the camera model error parameters and a simple as possible IP pipeline, it was decided to correct only for the bias. In the case of Dawn the bias was observed to have a slight dependency on the detector temperature (about 1.1 DN/K) and a spatial standard deviation across the pixel array of around 1.5 DN.[31] These effects were not characterized before launch, so just the pre-defined value of $\mathrm{DN}^{(0)} = 269$ is used.

Therefore, the DN measurement consists in the sum of the intensities of each pixel inside the ROI after bias subtraction:

$$\mathrm{DN} = \sum_{u,v}^{\mathrm{ROI}} (\mathrm{DN}_{u,v} - \mathrm{DN}^{(0)}) \tag{19}$$

where $\mathrm{DN}_{u,v}$ is the pixel value at row u and column v of the ROI.

Range Estimation

With the simplifications introduced previously, Eq. (8) can be rewritten for the Dawn scenario as:

$$d_i = \sqrt{\pi \, R_{\odot}^2 \, R^2 \, p_G \int_{\Delta\lambda} \mathrm{S}_1(\lambda) \, L_{\lambda_{\odot}}} \sqrt{\frac{\Psi(\alpha_i)}{d_{\odot_i}^2 \, \cos\epsilon_i \, \frac{\mathrm{DN}_i}{\Delta t_i}}} \tag{20}$$

The first square root term in the formula is a constant term, while the second term changes at every frame depending on the camera exposure time, the geometry of the scene and the image content.

The image content is returned by the IP module, while the geometry parameters for each frame are computed using Eqs. (9-10) and Eq. (15), as explained in the Methodology section. In the context of this experiment, the reconstructed attitude from SPICE kernels is used to simulate the estimated attitude at each frame, and no clock drift or bias is assumed on the epoch of the ephemeris evaluation. These effects are not included to avoid coupling their error with the range estimation error. In any case, they are not expected to contribute significantly to the range error. Concerning the LoS, the ROI centroid is used, without any phase angle correction. A phase angle different from zero would cause a bias in the LoS as the CoB of the body shifts away from the center of mass. However, correcting for phase angle would require the knowledge of this parameter, which is instead derived as output of Eq. (10) from the LoS itself in the current pipeline. In any case, the centroiding performance is not the focus of this work, and the positioning error caused by LoS error will be negligible with respect to the range error contribution, as it will be shown later.

The estimated range d, the absolute error $\delta d = d - d_{true}$, and the relative error $\delta\hat{d} = \delta d / d_{true}$ are shown in Fig. 4 and in Fig. 5 for the Vesta and Ceres approach, respectively. The true range d_{true} is assumed to be the one provided by SPICE kernels, which gives the best-available ground truth up to orbit determination errors. The discontinuities in the estimated range are due to the fact that, between each sequence, some days pass without any imaging operations.

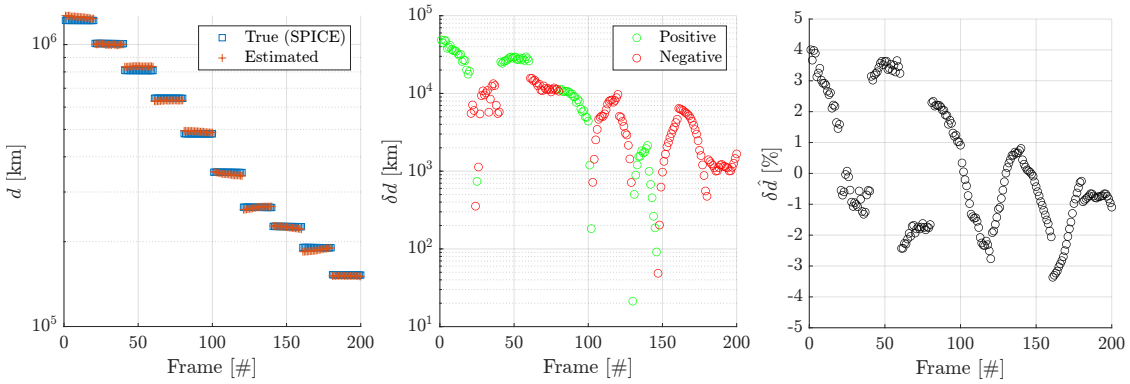

(a) Range estimation (b) Range estimation error (c) Relative range estimation error

Figure 4: Ranging performance for the Vesta scenario. The dataset comprises 10 sequences of 20 images each. Note: the range estimation error is shown in log scale, so the negative error is inverted in sign and labeled in red.

The performance remains under 4% in terms of relative range error for Vesta and under 1% for Ceres. This order of magnitude was expected as in-flight radiometric calibration accuracies have

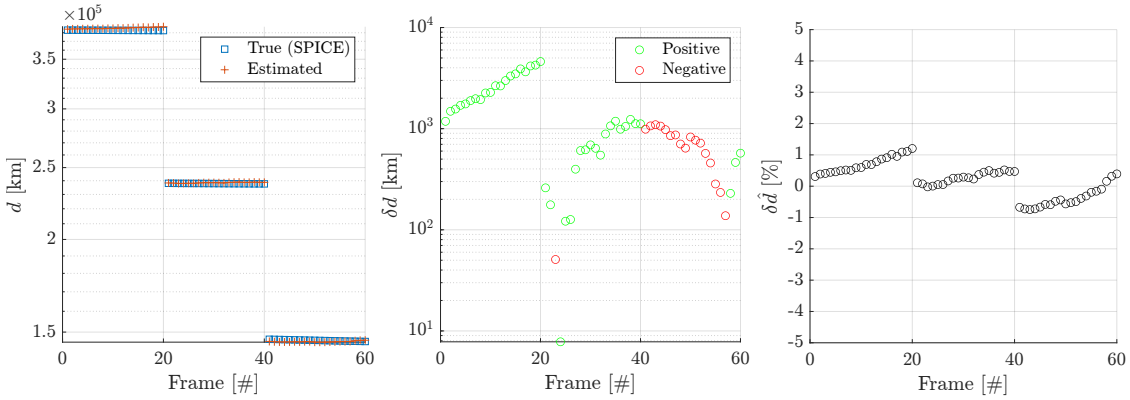

(a) Range estimation (b) Range estimation error (c) Relative range estimation error

Figure 5: Ranging performance for the Ceres scenario. The dataset comprises 3 sequences of 20 images each.

been assessed to be around 5% in several missions.[31,32,38–41] It is worth stressing that the errors shown refer to single-point kinematic solutions: the error could be smoothed and reduced over time by embedding the dynamics in an appropriate filter, as typically done in on-board implementations.[21]

To assess the multiplicative effect on the estimated range of the variables that vary over time in Eq. (20), each component is isolated and normalized to the value in the first frame. Fig. 6 shows that for the Vesta approach trajectory, the predominant contribution is given by the measured signal in DN/s, as expected by the steep range decrease throughout the dataset. The variation caused by off-pointing is negligible as the target is often aligned to the boresight and the FOV of the camera is narrow. On the other hand, the phase law and the distance of Vesta from the Sun should be known with good accuracy as they account for up to 15% and 1.5% in the change of the estimated value, respectively. It is worth noting that for a different scenario, such as during celestial triangulation, the predominant contribution could be given by the phase law instead of the signal itself, depending on the relative geometry between the probe and the beacon.

For the approach scenario, it is clear that the oscillations of the DN signal during a given sequence are the main cause of deviation of the estimated range from the ground truth. The period of these oscillations is linked with the relative spacecraft-target rotational motion. In particular, the relative error oscillations could be traced back to albedo heterogeneity and the irregular shape of the targets. In fact, the albedo used for the range estimation was considered as a constant uniform value, while the spacecraft observes different regions characterized by different local albedos while approaching the target. Moreover, the measurement model assumes a sphere with no local displacement, but this is not the case for the two targets. These effects would also explain why the error is lower for Ceres, which possesses a better sphericity and a more homogeneous albedo across its surface than Vesta. For example, the Rheasilvia basin of Vesta is about 10% brighter than the global average.[34] This claim will be later confirmed in the Synthetic Simulation section.

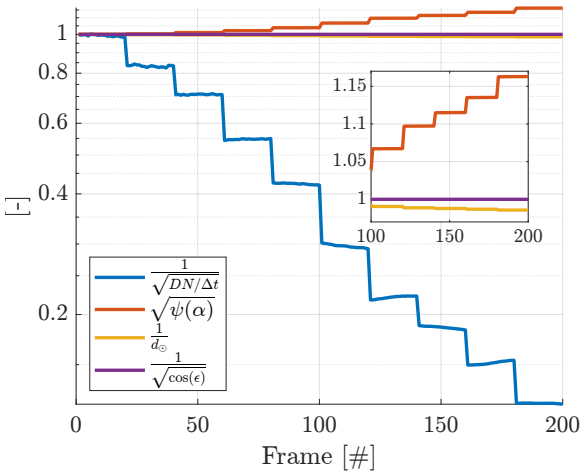

Figure 6: Contribution of the time-dependent geometry parameters to the range estimation for the Vesta scenario. The value taken by each parameter along the dataset is normalized to the value at the first frame to highlight the change in a relative scale.

Position Estimation

As shown in the Parameters Retrieval, by coupling the measured LoS with the estimated range, Dawn's relative position to the target can be obtained, as well as its inertial position from the Sun. The inertial positioning performance is reported in Fig. 7 and in Fig. 8 for Vesta and Ceres, respectively.

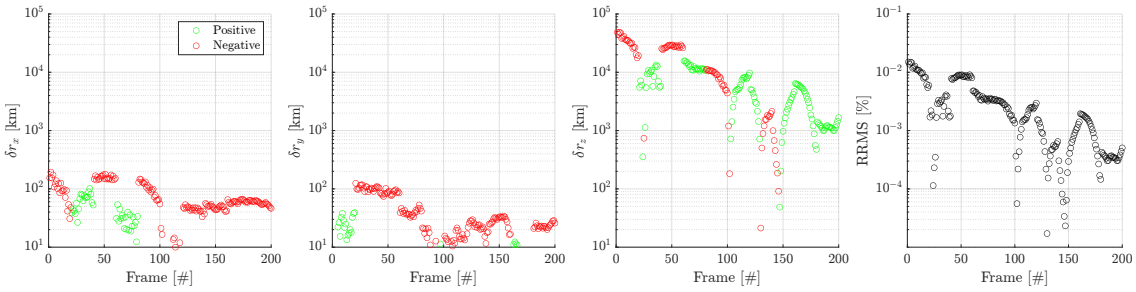

(a) Absolute error, X-axis (b) Absolute error, Y-axis (c) Absolute error, Z-axis (d) Relative RMS error

Figure 7: Positioning performance for the Vesta scenario. The estimated state is the position of Dawn from the Sun. The components are expressed in the camera frame (the boresight is aligned with the Z-axis).

The position vector is expressed in camera frame to highlight the range error contribution (Z-axis, i.e., boresight direction) with respect to the LoS error (X and Y axes). The boresight direction in conventional OpNav techniques has low observability due to the nature of the vision-based solution. In fact, systems are often equipped with an altimeter[15] or a lidar[16] to provide a measurement along this direction, or they fuse the LoS measurements with ground-station tracking. Radiometry-informed optical navigation provides a coarse albeit useful observable along this direction, hence enabling a full positioning solution without the need for redundant sensors.

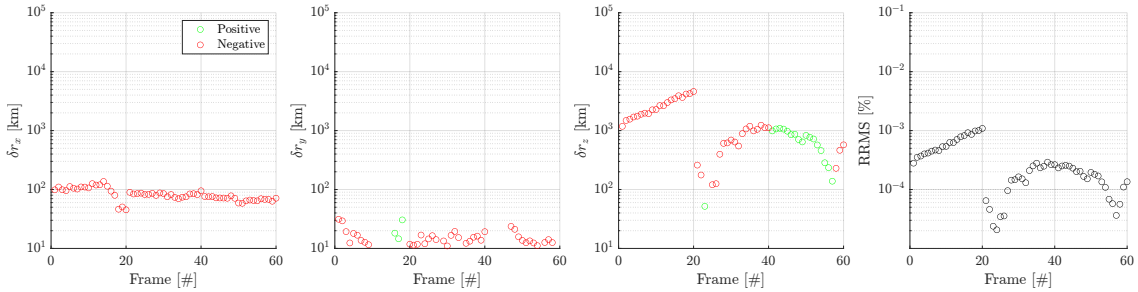

(a) Absolute error, X-axis (b) Absolute error, Y-axis (c) Absolute error, Z-axis (d) Relative RMS error

Figure 8: Positioning performance for the Ceres scenario.

In most of the data points, the range error is larger than the LoS error of at least one order of magnitude, as expected by the much larger uncertainties that enter into play when using radiometry ranging. However, in many frames the error drops to hundreds of km for both scenarios, which is in line with Deep-Space 1 filtered celestial triangulation performance of 700-1000 km.[6] Although this is an approach scenario and the body is closer and larger in the FOV, the results looks promising. It is worth noting that the centroiding performance are not discussed as they are not the focus of this work and they could likely be improved considering, for example, phase angle corrections, improving the overall performance as well.

Synthetic Simulation

A physically-based rendering simulation environment could enable the generation of synthetic images along the same approach trajectory, but using targets of different complexity. Such analysis could explain the oscillations observed in the relative error by separating them into components caused by specific features of the target.

To this aim, the Vesta scenario is recreated in ABRAM*. This render engine allows for high-quality radiometrically-consistent images thanks to its physically-based nature and the possibility of using high-resolution albedo and displacement maps, as well as a Hapke model and an accurate modeling of the camera response.[42,43]

The image generation pipeline is validated against close-range flight images acquired during the Rotational Characterization (RC) phase of Vesta. A comparison of a real flight image against the rendered counterpart is depicted in Fig. 9. An excellent match is obtained, which confirms the possibility of using the tool to recreate the approach imaging scenario.

The simulation comprises 9 different cases with different target complexities, as shown in Fig. 10. The most basic case is a perfect Lambertian sphere with uniform albedo. A first layer of complexity is the change of the shape, firstly from a sphere to an ellipsoid, then using a full displacement map. The second layer of complexity involves the albedo: instead of using a uniform albedo, the albedo map is employed, first with a simple Lambertian reflection model, then using the more realistic Hapke model. The highest-fidelity scenario has all the effects combined and is truthful to reality, matching the real flight images.

*github.com/andrepiz/abram

(a) Real image (b) ABRAM rendering

Figure 9: Qualitative validation of the synthetic image generation pipeline. Zoomed insets have been added to the pictures to highlight the accuracy in the rendering of lights and shadows from the render engine.

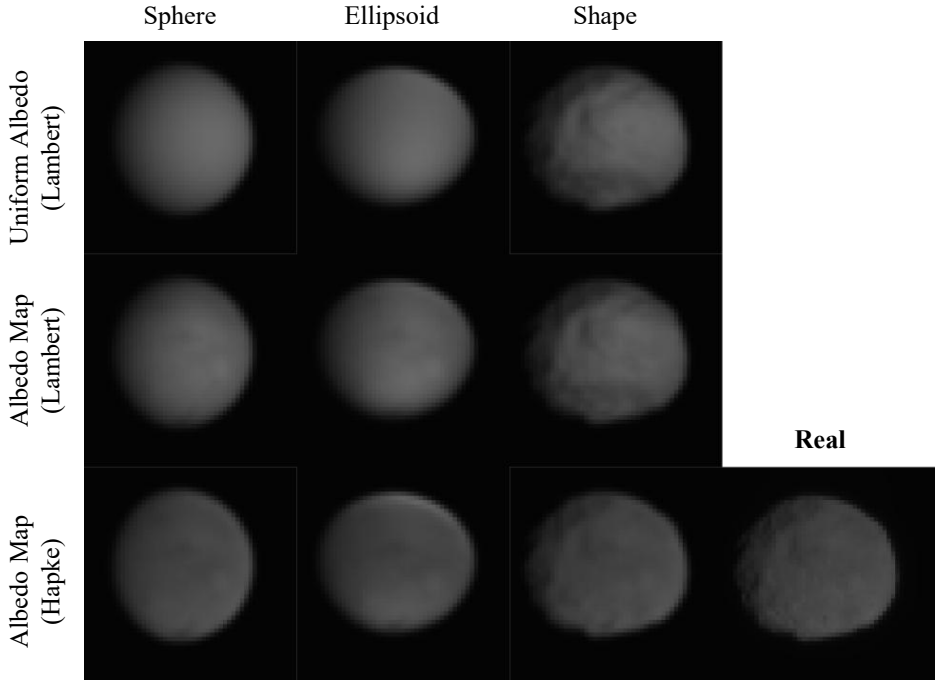

Figure 10: Overview of the datasets of synthetic images produced. 9 targets of different complexity are simulated, with incremental addition of features for each case.

The range estimation pipeline is run across all these scenarios. The plot in Fig. 11 depicts how each feature contributes to the overall relative error with its own effects. The baseline case is the perfect sphere, where the error is zero as all the model assumptions are respected. The shape effects mainly cause a drift of the error, with some minor oscillations that offset from the mean error trend. Interestingly, the difference between the full shape model and the ellipsoid model is not small, i.e., an ellipsoid is not a good approximation for the effects caused by shadows and occlusions. The albedo map introduces larger oscillations than the shape features, but not a recognizable drift. Moreover, a Lambertian target generally returns errors that are more bounded than an Hapke model, owing to the lower complexity of the Lambert reflection model and its phase law. Finally, when all the features are combined, the highest fidelity model returns a relative error that matches the one obtained previously with the real images.

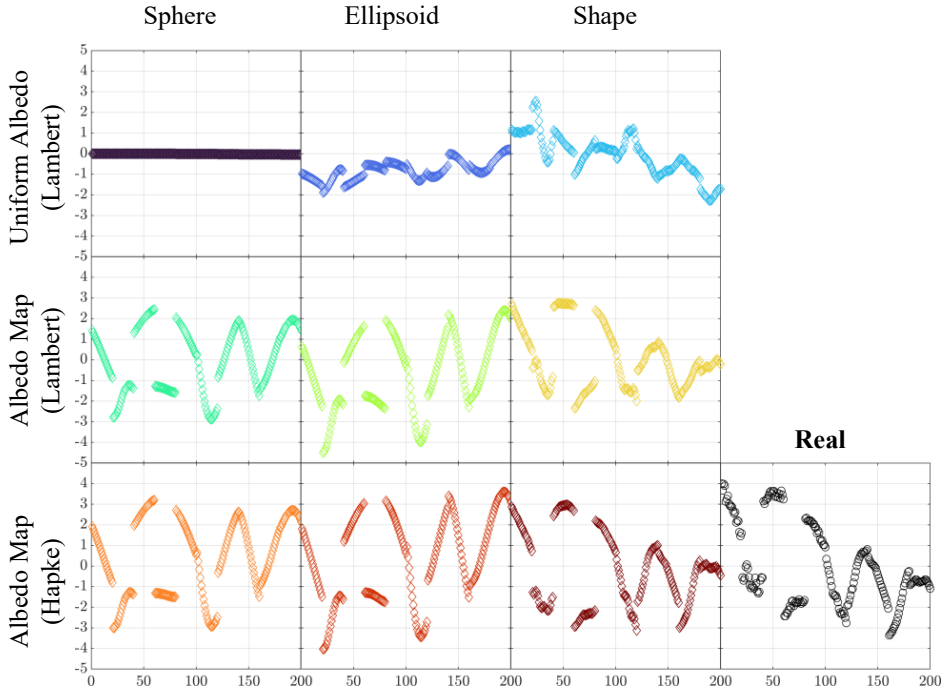

Figure 11: Relative range error obtained using different datasets of synthetic images. The error drifts or oscillates differently depending on the complexity of the target body. A perfect Lambertian sphere returns zero error, while the error obtained with the highest fidelity model is both drifting and oscillating, and it matches the trend of the real image dataset.

These findings suggest that the amplitude of oscillations could be lower for targets with a more homogeneous albedo distribution or characterized by a smoother spherical surface, such as airless planets.

A residual difference is also present in the error obtained with the highest-fidelity synthetic model, bounded between -3% and 3%, and the real images, bounded between -4% and 4%. This difference could likely be explained by the presence of noise in the real images, which is not present in the synthetic images. Dark current, smear, flat field variations, and in-field stray light were not compensated for and might have a non-negligible contribution to the error. For future works, it could be beneficial to investigate their impact using radiometrically-calibrated images (i.e., radiance images),

instead of raw DN files. This consideration applies as well to light-effect perturbations, including light-time delays and light aberrations.[44] Although these last effects are expected to play a negligible role considering the current model performance, a generalized formulation that accounts for all these error sources may be beneficial to develop and is deferred to future work.

Finally, there might be the possibility to correct for these features by using, for example, a varying geometric albedo or a changing radius depending on the relative spacecraft-target rotational state. The error could be reduced by exploiting the albedo map, the shape, and the rotational state directly in the estimation, if these are known from, e.g., a mission that already flew to that body.

CONCLUSIONS

This study assessed the feasibility of using pixel intensities as an observable to estimate the range, hence the position (when coupled with the LoS) of the observer. Applied to the space navigation scenario, the presented method provides a full 3D state estimation solution without a priori knowledge of the probe state and using a single image of a known target illuminated by the Sun. Using precise radiometric models and thorough camera calibration, it is demonstrated how to estimate the range and reconstruct the spacecraft position with a small knowledge of the scene geometry - specifically, the target ephemeris and the inertial camera orientation - and a simple image processing pipeline.

Validation with Dawn spacecraft flight imagery during its approach to Vesta and Ceres shows a range relative error performance throughout the dataset below 4% and 1%, respectively, confirming the feasibility of the technique for interplanetary navigation under realistic operating conditions. Surface albedo heterogeneity and irregular shape are the main causes of error oscillations, as confirmed by the performance obtained on synthetic images in the same scenario but generated using targets of different feature complexity.

Radiometry-informed navigation removes the operational constraint of conventional celestial triangulation techniques, which require multiple beacons in view for a feasible solution. The technique can also be used to support state estimation during approach trajectories to known bodies, when ground-station tracking or redundant sensors are not available. Collectively, these findings indicate that radiometry-informed optical navigation represents an advancement toward greater autonomy in space exploration missions.

FUNDING SOURCES

The PhD scholarship of A.P. is sponsored by The European Union under the NextGenerationEU (NGEU) programme (Mission 4, Component 1, CUP \D43C23002190008).

P.P. and F.T. are sponsored by EXTREMA, a project that has received funding from the European Research Council (ERC) under the European Union's Horizon 2020 research and innovation programme (Grant Agreement No.\864697).

ACKNOWLEDGMENTS

A.P. would like to acknowledge the support received by Shyam Bhaskaran during its visiting research period at Jet Propulsion Laboratory.

REFERENCES

[1] N. Jerath and H. Ohtakay, "Mariner IX optical navigation using Mars lit limb," *Journal of Spacecraft and Rockets*, Vol. 11, No. 7, 1974, pp. 505–511.

[2] R. Stanton, H. Ohtakay, J. Miller, and C. Voge, "Demonstration of optical navigation measurements on Mariner 10," *13th Aerospace Sciences Meeting*, 1975, p. 86.

[3] R. VAUGHAN, J. RIEDEL, R. DAVIS, W. OWEN, JR., and S. SYNNOTT, "Optical navigation for the Galileo Gaspra encounter," Aug. 1992.

[4] D. L. Matson, L. J. Spilker, and J.-P. Lebreton, "The Cassini/Huygens mission to the Saturnian system," *Space Science Reviews*, Vol. 104, No. 1, 2002, pp. 1–58.

[5] C. Kohlhase and P. A. Penzo, "Voyager mission description," *Space science reviews*, Vol. 21, No. 2, 1977, pp. 77–101.

[6] S. Bhaskaran, J. Riedel, S. Synnott, and T. Wang, "The Deep Space 1 autonomous navigation system - A post-flight analysis," Aug. 2000.

[7] S. Bhaskaran, N. Mastrodemos, J. E. Riedel, and S. P. Synnott, "Optical navigation for the stardust wild 2 encounter," *Proceedings of the 18th International Symposium on Space Flight Dynamics (ESA SP-548). Jointly organised by the German Space Operations Center of DLR and the European Space Operations Centre of ESA. 11-15 October 2004, Munich, Germany., p. 455*, Vol. 548, 2004, p. 455.

[8] O. Camino, M. Alonso, D. Gestal, J. d. Bruin, P. Rathsman, J. Kugelberg, P. Bodin, S. Ricken, R. Blake, P. P. Voss, *et al.*, "SMART-1 operations experience and lessons learnt," *Acta Astronautica*, Vol. 61, No. 1-6, 2007, pp. 203–222.

[9] F. Castellini, D. Antal-Wokes, R. P. d. Santayana, and K. Vantournhout, "Far approach optical navigation and comet photometry for the rosetta mission," *Proceedings of the 25th International Symposium on Space Flight Dynamics (ISSFD'15)*, 2015.

[10] N. Mastrodemos, B. Rush, A. Vaughan, and W. Owen, "Optical navigation for the Dawn mission at Vesta," *23rd International Symposium on Space Flight Dynamics, Pasadena, CA*, Vol. 29, 2012.

[11] R. B. Frauenholz, R. S. Bhat, S. R. Chesley, N. Mastrodemos, W. M. Owen Jr, and M. S. Ryne, "Deep impact navigation system performance," *Journal of Spacecraft and Rockets*, Vol. 45, No. 1, 2008, pp. 39–56.

[12] J. Bellerose, S. Bhaskaran, B. Rush, Z. Tarzi, D. Velez, D. Mages, A. Vaughan, F. Laipert, J. Atchison, M. McQuaide, *et al.*, "Double asteroid redirection test (DART): navigating to obliteration," *Acta Astronautica*, Vol. 219, 2024, pp. 417–427.

[13] R. Inman, G. Holt, J. Christian, K. W. Smith, and C. D'Souza, "Artemis I optical navigation system performance," *AIAA SCITECH 2024 Forum*, 2024, p. 0514.

[14] E. Ecale, F. Torelli, and I. Tanco, "JUICE interplanetary operations design: drivers and challenges," *2018 SpaceOps Conference*, 2018, p. 2493.

[15] A. Pellacani, M. Graziano, M. Fittock, J. Gil, and I. Carnelli, "HERA vision based GNC and autonomy," *Proceedings of the 8th European Conference for Aeronautics and Space Sciences. Madrid, Spain, 1-4 july 2019*, 2019.

[16] M. Pugliatti, F. Piccolo, A. Rizza, V. Franzese, and F. Topputo, "The vision-based guidance, navigation, and control system of Hera's Milani Cubesat," *Acta Astronautica*, Vol. 210, 2023, pp. 14–28.

[17] S. B. Broschart, N. Bradley, and S. Bhaskaran, "Kinematic approximation of position accuracy achieved using optical observations of distant asteroids," *Journal of Spacecraft and Rockets*, Vol. 56, No. 5, 2019, pp. 1383–1392.

[18] S. Henry and J. A. Christian, "Absolute triangulation algorithms for space exploration," *Journal of Guidance, Control, and Dynamics*, Vol. 46, No. 1, 2023, pp. 21–46.

[19] R. Raymond Karimi and D. Mortari, "Interplanetary autonomous navigation using visible planets," *Journal of Guidance, Control, and Dynamics*, Vol. 38, No. 6, 2015, pp. 1151–1156.

[20] V. Franzese, F. Topputo, F. Ankersen, and R. Walker, "Deep-space optical navigation for M-ARGO mission," *The Journal of the Astronautical Sciences*, Vol. 68, No. 4, 2021, pp. 1034–1055.

[21] E. Andreis, P. Panicucci, and F. Topputo, "Autonomous Vision-Based Algorithm for Interplanetary Navigation," *Journal of guidance, control, and dynamics*, Vol. 47, No. 9, 2024, pp. 1792–1807.

[22] V. Franzese and F. Topputo, "Optimal beacons selection for deep-space optical navigation," *The Journal of the Astronautical Sciences*, Vol. 67, No. 4, 2020, pp. 1775–1792.

[23] S. Bhaskaran, "Autonomous optical-only navigation for deep space missions," *ASCEND 2020*, p. 4139, 2020.

[24] E. Andreis, V. Franzese, and F. Topputo, "Onboard orbit determination for deep-space cubesats," *Journal of guidance, control, and dynamics*, Vol. 45, No. 8, 2022, pp. 1466–1480.

[25] I. A. Nesnas, B. J. Hockman, S. Bandopadhyay, B. J. Morrell, D. P. Lubey, J. Villa, D. S. Bayard, A. Osmundson, B. Jarvis, M. Bersani, *et al.*, "Autonomous exploration of small bodies toward greater autonomy for deep space missions," *Frontiers in Robotics and AI*, Vol. 8, 2021, p. 650885.

[26] S. Bhaskaran, J. E. Riedel, and S. P. Synnott, "Autonomous target tracking of small bodies during flybys," 2004.

[27] U. S. N. B. o. Standards and F. E. Nicodemus, *Geometrical considerations and nomenclature for reflectance*, Vol. 160. US Department of Commerce, National Bureau of Standards Washington, DC, USA, 1977.

[28] T. P. Lester, M. L. McCall, and J. Tatum, "Theory of planetary photometry," *Journal of the Royal Astronomical Society of Canada, vol. 73, Oct. 1979, p. 233-257.*, Vol. 73, 1979, pp. 233–257.

[29] A. Mallama, B. Krobusek, and H. Pavlov, "Comprehensive wide-band magnitudes and albedos for the planets, with applications to exo-planets and Planet Nine," *Icarus*, Vol. 282, 2017, pp. 19–33.

[30] J. M. Palmer and B. G. Grant, "The art of radiometry," 2009.

[31] G. Kovács, A. Nathues, H. Sierks, P. Gutiérrez Marqués, M. Hoffmann, and G. S. Thangjam, "The scientific calibration of the dawn framing camera," *Space Science Reviews*, Vol. 220, No. 1, 2024, p. 4.

[32] S. Schröder, T. Maue, P. G. Marqués, S. Mottola, K. Aye, H. Sierks, H. Keller, and A. Nathues, "In-flight calibration of the Dawn Framing Camera," *Icarus*, Vol. 226, No. 2, 2013, pp. 1304–1317.

[33] H. Sierks, H. Keller, R. Jaumann, H. Michalik, T. Behnke, F. Bubenhagen, I. Büttner, U. Carsenty, U. Christensen, R. Enge, *et al.*, "The Dawn framing camera," *Space science reviews*, Vol. 163, No. 1, 2011, pp. 263–327.

[34] J.-Y. Li, L. Le Corre, S. E. Schröder, V. Reddy, B. W. Denevi, B. J. Buratti, S. Mottola, M. Hoffmann, P. Gutierrez-Marques, A. Nathues, *et al.*, "Global photometric properties of asteroid (4) Vesta observed with Dawn framing camera," *Icarus*, Vol. 226, No. 2, 2013, pp. 1252–1274.

[35] J.-Y. Li, S. E. Schröder, S. Mottola, A. Nathues, J. C. Castillo-Rogez, N. Schorghofer, D. A. Williams, M. Ciarniello, A. Longobardo, C. A. Raymond, *et al.*, "Spectrophotometric modeling and mapping of Ceres," *Icarus*, Vol. 322, 2019, pp. 144–167.

[36] B. Hapke, "Bidirectional reflectance spectroscopy: 1. Theory," *Journal of Geophysical Research: Solid Earth*, Vol. 86, No. B4, 1981, pp. 3039–3054.

[37] B. Hapke, "Bidirectional reflectance spectroscopy: 6. Effects of porosity," *Icarus*, Vol. 195, No. 2, 2008, pp. 918–926.

[38] E. Tatsumi, T. Kouyama, H. Suzuki, M. Yamada, N. Sakatani, S. Kameda, Y. Yokota, R. Honda, T. Morota, K. Moroi, *et al.*, "Updated inflight calibration of Hayabusa2's optical navigation camera (ONC) for scientific observations during the cruise phase," *Icarus*, Vol. 325, 2019, pp. 153–195.

[39] B. Bos, D. Nelson, J. Pelgrift, A. Liounis, D. Doelling, C. Norman, R. Olds, C. May, R. Witherspoon, E. Church, *et al.*, "In-flight calibration and performance of the OSIRIS-REx touch and go camera system (TAGCAMS)," *Space Science Reviews*, Vol. 216, No. 4, 2020, p. 71.

[40] B. Geiger, R. Andrés, and T. Statella, "Radiometric Calibration of the Rosetta Navigation Camera," *Journal of Astronomical Instrumentation*, Vol. 10, No. 01, 2021, p. 2150004.

[41] C. M. Ernst, R. T. Daly, Z. J. Fletcher, K. J. Ryan, A. F. Cheng, S.-Y. W. Hsieh, T. L. Farnham, C. A. Sawyer, A. K. Glantzberg, O. S. Barnouin, *et al.*, "Calibration and In-flight Performance of DART's Didymos Reconnaissance and Asteroid Camera for OpNav (DRACO)," *The Planetary Science Journal*, Vol. 5, No. 11, 2024, p. 257.

[42] A. Pizzetti, P. Panicucci, and F. Topputo, "A Radiometric Consistent Render Procedure for Planets and Moons," *4th Space Imaging Workshop*, 2024, pp. 1–3.

[43] A. Pizzetti, P. Panicucci, F. Capolupo, and F. Topputo, "Development and Validation of a Physically-Based Rendering Methodology for Celestial Bodies," *Acta Astronautica*, 2026.

[44] M. D. Shuster, "Stellar aberration and parallax: a tutorial," *The Journal of the astronautical sciences*, Vol. 51, No. 4, 2003, pp. 477–494.

[45] B. Hapke, "Bidirectional reflectance spectroscopy 7: The single particle phase function hockey stick relation," *Icarus*, Vol. 221, No. 2, 2012, pp. 1079–1083.

[46] B. Hapke, "Bidirectional reflectance spectroscopy: 3. Correction for macroscopic roughness," *Icarus*, Vol. 59, No. 1, 1984, pp. 41–59.

APPENDIX A: HAPKE PHASE LAW

In this work, an Hapke reflection model without Coherent-Backscattering Opposition Effect (CBOE) and without porosity effects is employed. Its phase law is:[36]

$$\Psi(\alpha) = K(\alpha,\theta)\frac{r_0}{2\,p_G}\left[\left(\frac{1+\gamma^2}{4}\big(\,(1+B(\alpha))\,P(\alpha)-1\big)+(1-r_0)\right)\right.$$
$$\left.\times\left(1-\sin\frac{|\alpha|}{2}\tan\frac{|\alpha|}{2}\ln\cot\frac{|\alpha|}{4}\right)+\frac{4}{3}r_0\frac{\sin\alpha+(\pi-\alpha)\cos\alpha}{\pi}\right] \tag{21}$$

where p_G is the geometric albedo, which for an Hapke model can be written as:[36]

$$p_G = C(w,\theta)\frac{r_0}{2}\left(1+\frac{r_0}{3}\right)+\frac{w}{8}\left((1+B_0)\,P(0)-1\right) \tag{22}$$

r_0 is defined as:

$$r_0 = \frac{1-\gamma}{1+\gamma} \tag{23}$$

with:

$$\gamma = \sqrt{1-w} \tag{24}$$

where w is the Single-Scattering Albedo (SSA).

$B(\alpha)$ is the Shadow-Hiding Opposition Effect (SHOE):

$$B(\alpha) = 1 + B_0\,\frac{1}{1+\frac{\tan(\alpha/2)}{h}} \tag{25}$$

where B_0 is the SHOE amplitude and h the SHOE width, and $P(\alpha)$ is the Single-Particle Phase Function (SPPF):[45]

$$P(\alpha) = \frac{1+c}{2}\,\frac{1-b^2}{(1-2b\cos\alpha+b^2)^{3/2}}+\frac{1-c}{2}\,\frac{1-b^2}{(1+2b\cos\alpha+b^2)^{3/2}} \tag{26}$$

where a double-term Henyey-Greenstein (HG) function is used with shape parameter b and asymmetry parameter c.

Finally, $K(\alpha,\theta)$ and $C(w,\theta)$ are empirical functions to account for the macroscopic roughness θ. The reader is redirected to Ref. 46 for the formulation of these two terms.